

Article

Microstructure, Mechanical Properties and Fire Resistance of High Strength Mg-Gd-Y-Zr Alloys

Yafeng Qian ^{1,*}, Yanhui Zhao ^{1,*}, Xiaorui Dong ², Wei Yu ^{3,*}, Jianhang Feng ⁴ and Hui Yu ⁴

¹ National Quality Supervision and Inspection Center for Magnesium and Magnesium Alloy Products, Hebi 458030, China

² College of Materials Science and Engineering, Jilin University, Changchun 130022, China

³ School of Materials Science and Engineering, Hefei University of Technology, Hefei 230009, China

⁴ School of Materials Science and Engineering, Hebei University of Technology, Tianjin 300130, China

* Correspondence: ncqsimagnesium@126.com (Y.Z.); yuwei52213@163.com (W.Y.)

Abstract: With the lightest green structural material for 21st century, a significant weight reduction effect was expected to solve the lightweight problem in aerospace and other fields. However, the material's poor mechanical properties and flammability limited its widely application in such fields. In this paper, the GWK series alloys (Mg-5.3Gd-4.11Y-0.13Zr, Mg-5.5Gd-4.22Y-0.19Zr, and Mg-5.46Gd-4.02Y-0.20Zr, in wt.%) were designed, and we explored the effect of alloy composition and process on the microstructure and properties of GWK series alloys subject to casting, homogenization, extrusion, ageing and ignition. The result show that Mg-5.3Gd-4.11Y-0.13Zr alloy after T4 treatment at 500 °C/6 h obtains an excellent solid solution effect. In addition, the aged alloy shows a good balance of mechanical properties, a tensile strength of 405 MPa, yield strength of 275 MPa, as well as elongation of 8.12%, and excellent non-flammability.

Keywords: Mg-Gd-Y-Zr alloy; non-flammability; extrusion; microstructure; mechanical properties



Citation: Qian, Y.; Zhao, Y.; Dong, X.; Yu, W.; Feng, J.; Yu, H.

Microstructure, Mechanical

Properties and Fire Resistance of High Strength Mg-Gd-Y-Zr Alloys.

Metals **2022**, *12*, 1456. <https://doi.org/10.3390/met12091456>

Academic Editors: Jianyue Zhang and Alan Luo

Received: 6 July 2022

Accepted: 18 August 2022

Published: 30 August 2022

Publisher's Note: MDPI stays neutral with regard to jurisdictional claims in published maps and institutional affiliations.



Copyright: © 2022 by the authors. Licensee MDPI, Basel, Switzerland. This article is an open access article distributed under the terms and conditions of the Creative Commons Attribution (CC BY) license (<https://creativecommons.org/licenses/by/4.0/>).

1. Introduction

Excessive use and insufficient reserves of fossil fuels have driven the demand for new energy and new materials in the manufacturing industry, especially in the fields of automobiles, railways and aerospace. How to achieve higher fuel efficiency, reduce carbon emissions, and gradually achieve carbon neutrality has become a top priority [1–3]. Compared with steel materials, magnesium alloys, as the lightest metal structural materials, have attracted much attention because of their high specific strength, specific stiffness, good castability and good damping and vibration reduction [4,5]. At present, in the aerospace field, magnesium alloys have been widely used in structural parts such as aircraft, missiles, spaceships, satellites, etc. their good weight reduction benefits not only help improve the maneuverability and transportation capacity of aircraft, but also significantly reduce transportation costs. [6–8]. However, compared with other lightweight metal structural materials (such as titanium alloys and aluminum alloys), the active chemical properties of magnesium make it prone to corrosion and oxidation in high-temperature atmospheric environments, and the Pilling-Bedworth of the initial MgO layer formed during the oxidation process is low and easy to crack, thereby accelerating the subsequent oxidation of the magnesium matrix [9]. Traditional commercial magnesium alloys (such as AZ31, AZ80 and ZE41) have poor oxidation resistance, easy surface degradation under long-term high temperature exposure, and easy combustion when exposed to sufficient heat sources or flames, especially in the cabin environment [10]. In addition, the close-packed hexagonal structure of magnesium alloys limits the number of start-up slip systems and start-up energy barriers for room temperature deformation, which makes it difficult to meet the demand for high-strength and tough structural materials in aerospace [11].

Therefore, the development of magnesium alloys with both high strength and toughness and high flame retardancy is of great significance for expanding applications.

In recent years, the United States Federal Aviation Administration (FAA) has conducted flammability tests on new rare-earth magnesium alloys and found that rare-earth magnesium alloys have better flame retardant properties than aluminum alloys [10]. The results show that the combustion characteristics and combustion mechanism of magnesium alloys are closely related to the characteristics of the alloy itself (thermophysical properties, oxide film properties, chemical composition, geometric dimensions, etc.) and the external environment (gas type, oxygen concentration and pressure, etc.) [9,12]. Generally speaking, the combustion of magnesium alloys is related to the failure of its high temperature oxide film. From the perspective of thermodynamics, the change of Gibbs free energy directly affects the oxidation film formation and its stability. If the Gibbs free energy change of the oxide film formation reaction is affected by alloying, the dense oxide film is preferentially formed outside the magnesium oxide, which effectively prevents the magnesium matrix from burning. Although rare-earth elements such as cerium [13,14], rare-earth element calcium [15–17], and other oxide formation reactions have positive Gibbs free energy, they can form a dense oxide film inside the MgO oxide film to prevent further oxidation reactions. The addition of beryllium [15,16], yttrium [16], and other elements significantly affects the oxide film of magnesium alloys, obtaining multi-layer dense oxide film structures such as BeO and Y₂O₃, and thereby improving the oxidation resistance of magnesium alloys. In addition, the flame retardant properties of magnesium alloys can also be improved by surface treatment methods such as the spraying of flame retardant materials. However, due to the technical difficulty, cost, and application limitations of surface treatment, the use of alloying methods to control the composition and structure of magnesium alloy oxide films has become a simpler and more efficient way to improve the flame retardant properties of magnesium alloys. In addition to the low flame retardant performance, low strength is also an important factor limiting the application of magnesium alloy materials in the aerospace field. In general, rare-earth alloying combined with large plastic deformation methods has become a key method for the preparation of ultra-high strength magnesium alloy materials. Pan [18] aimed at Mg-13Gd alloy, and the yield strength of the material produced by extrusion composite aging process was as high as 470 MPa. Liu [19] added yttrium and zirconium elements on the basis of an Mg-Gd alloy system and prepared Mg-8Gd-3Y-0.4Zr alloy by rotary forging and aging, which further increased the yield strength of the material to 650 MPa. Based on this, in this paper, aiming at the Mg-Gd-Y-Zr (GWK) alloy system, through the alloy composition design, a low-cost magnesium rare-earth alloy was successfully prepared by the traditional extrusion composite aging heat treatment process, and its strengthening, toughening and combustion mechanism were investigated. The research and discussion provide data support and useful reference for the key preparation of low-cost aerospace magnesium alloys.

2. Experiment and Method

2.1. Experimental Materials

In general, the performance requirements of metal structural materials for aerospace seats [10] are as follows: the breaking strength (TS) reaches 400 MPa, the strength does not drop by more than 20% at 250 °C, and the density is <2 g/cm³. At present, the magnesium alloy systems that meet the requirements of the above indicators are mostly concentrated in rare-earth composite strengthened magnesium alloys [11], but the addition of a large amount of rare-earth elements leads to a significant increase in the cost of alloy preparation. Previous studies have found that the aging strengthening effect of the element Gd is stronger than that of the element Y. Therefore, under the premise of reducing the total amount of rare earth elements, this paper designs three new GWK magnesium alloys with different compositions, containing 5.3–5.6 wt.% Gd, 4–4.2 wt.% Y, and 0.13–0.2 wt.% Zr. Considering the yield of rare-earth elements in smelting, the intermediate alloy addition method is adopted, and the yield of each element was Gd: 70–75%, Y: 50–55%, Zr: 15–25%.

The specific raw materials are high-purity magnesium ($Mg > 99.99\%$), Mg-30Gd, Mg-30Y, and Mg-30Zr master alloys.

2.2. Alloy Preparation

The ingots were prepared using high purity magnesium (99.99%) Mg-30Gd (wt.%), Mg-30Y (wt.%), and Mg-30Zr master alloy, which were preheated at 200 °C for 20 min and melted at 730–780 °C in steel crucibles under a gas mixture CO_2 and SF_6 to avoid molten oxidation. Through stirring with Ar gas for 5 min to remove the slag and standing for 10 min, the molten was poured at 720–730 °C and 55 mm/min to obtain a $\Phi 100$ mm semi-continuous ingot.

Because the addition of Y and Zr elements affects the precipitation behavior of Mg-Gd alloys, this paper used Pandat software to calculate and determine the optimal homogenization treatment plan [20]. After heat treatment, the sample was machined to $\Phi 95$ mm for use. In order to illustrate the effect of trace changes of alloying elements, a $\Phi 19$ mm extrusion die was used, the extrusion ratio were 25:1, and the die was preheated to 430 °C for extrusion. The $\Phi 23$ mm bar die was extruded at 430 °C, the extrusion ratio were 25:1 and 17:1, the extrusion speed was 3–5 mm/s, and the extrusion is naturally cooled. The aging treatment conditions were: aging temperature 200 °C; time 12 h, 24 h, 64 h; and 72 h; and air cooling.

2.3. Tissue Characterization and Performance Testing

The composition was measured in three areas along the length direction of the semi-continuous cast rod and the middle and the lower parts. The inspection unit was the National Light Metal Quality Supervision and Inspection Center, using an electronic balance and an inductively coupled plasma atomic emission spectrometer (ICP-AES), according to GB/T 13748.20-2009 Standard implementation. Alloy density was measured using the Archimedes drainage method with an accuracy of 0.1 mg and 1 mL. The modulus was determined by ultrasonic method, and the Young's modulus, shear modulus and bulk elastic modulus of the material were obtained by measuring the propagation velocity of longitudinal and transverse waves in the solid. Sampling locations were different for as-cast, solution, as-extruded, and aged alloys. Among them, the as-cast alloy was sampled at the core and edge along the cooling direction; the cross-section of the as-extruded alloy was observed along the extrusion direction; the samples after the combustion test were sampled from the same positions at the top, middle, and bottom of the burning sample. All samples were polished with different mesh sandpapers in turn and then polished with diamond. The metallographic etching solution was a mixture of 10 mL acetic acid + 4.2 g picric acid + 70 mL ethanol + 10 mL distilled water, and the microstructure was observed with an OLYCIA M3 optical microscope, according to the standards GB/T 4296-2004 and GB/T 4297-2004. UTM5105G universal testing machine was used to test the mechanical properties. The samples in each state were tested 3 times and the median value was taken. Refer to GB/T 228.1-2010 for implementation. The as-cast, as-extruded and aged alloy flammability test samples were solid cone-shaped cylinders with a diameter of 0.85 mm and heights of 38.1 mm, and 254 mm at the top and bottom, respectively, and the size of the assembly plug hole was $\Phi 6.35$ mm \times 50.8 mm, as shown in Figure 1. The fuel combustion device and test samples were in accordance with the US Federal Aviation Administration (FAA) standard [10].

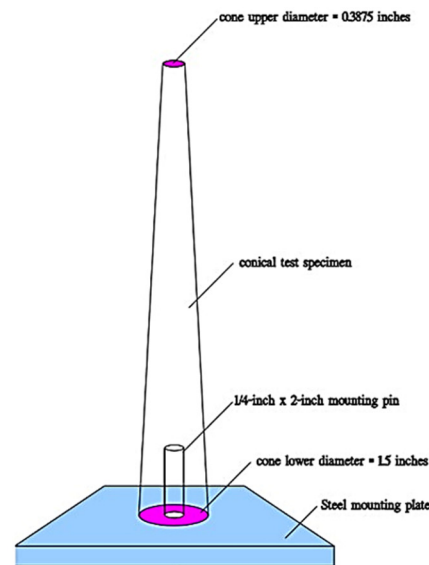


Figure 1. Sketch diagram of flammability test.

3. Results and Discussion

3.1. Microstructure of as-cast Alloy

In order to verify the casting alloy yield and billet quality stability, three semi-continuous castings were compared in this paper, which were distinguished as a, b, and c, respectively. In Table 1, the chemical composition of the upper, middle, and lower parts of the alloy in the three tests is basically the same as the design value, and the theoretical density and the measured density are also very similar, indicating that the casting and pouring process of the GWK alloy is stable and reliable, and the composition is uniform.

Table 1. Actual composition and density of as-cast GWK alloys.

Samples	Alloys Element (in wt.%)			Designed Density (g/cm ³)	Actual Density (g/cm ³)
	Gd	Y	Zr		
GWK-a	5.29/5.41/5.20 (5.30)	4.14/4.20/3.98 (4.11)	0.13/0.13/0.14 (0.13)	1.866	1.84
GWK-b	5.51/5.44/5.56 (5.50)	4.25/4.14/4.27 (4.22)	0.19/0.19/0.20 (0.19)	1.890	1.86
GWK-c	5.42/5.58/5.38 (5.46)	4.06/4.13/3.88 (4.02)	0.20/0.19/0.21 (0.20)	1.868	1.84

From Figure 2 we can see that the industrially produced as-cast GWK alloys of the three components are all composed of primary dendrites and eutectics, and the magnesium rare-earth compounds are mainly precipitated at the grain boundaries. However, there are some differences between the core and the edge at the same positions. The dendrite spacing in the external microstructure of the alloy is reduced, and the grain size is also smaller than that in the core. This is because the metal solution has a large temperature gradient inside the ingot mold and the mold temperature is low, so the surface metal is affected by the ingot mold. Severe supercooling results in a fine-grained structure, while the metal liquid near the center has a smaller temperature gradient, so the grains are relatively coarse at the center. Moreover, compared the difference in trace addition of Zr between the as-cast alloys (GWK-a, b, c), the amount of inclusion would increase with the addition of Zr increasing for as-cast GWK alloys. Figure 3 shows that the eutectic compounds of the three alloys are mostly distributed at the grain boundary in the form of strips, the size of each eutectic compound is not very different, and most of them show a trend of decreasing size with the

decrease of cooling rate. In addition, some inclusions were also found in the GWK-b and -c samples, which may be caused by the strong stirring to reduce the element burning loss when the rare-earth addition amount is high.

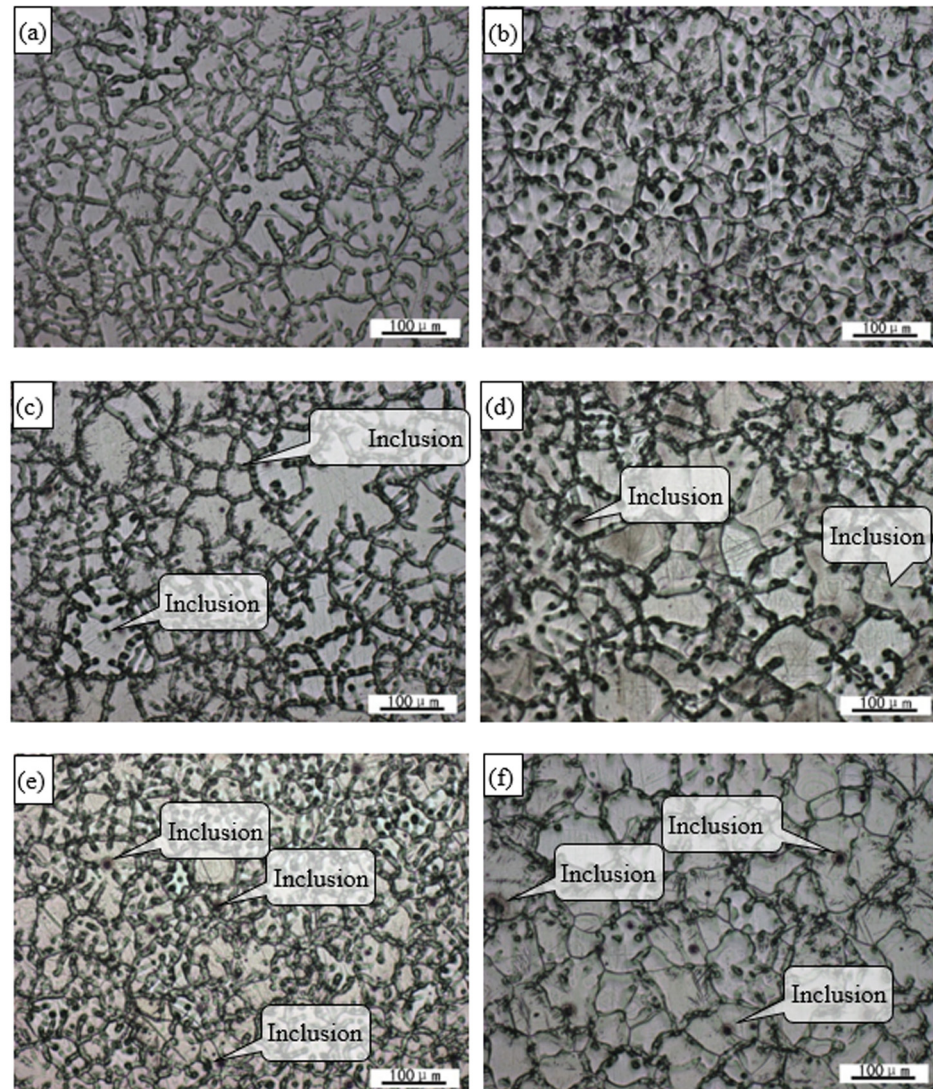


Figure 2. Optical microstructure of various GWK alloys from the center and edge of (a,b) GWK-a ingot; (c,d) GWK-b ingot; (e,f) GWK-c ingot.

3.2. Alloy Precipitation Behavior and Homogenized Microstructure

It can be seen from Figure 4a that, relative to the equilibrium phase diagram of the Mg-Gd alloy, as the Y content increases from 4 wt.% to 4.2 wt.%, the α -Mg eutectoid reaction temperature shifts to the right, and the α -Mg + Mg_5Gd is two-phased. The three-phase region of α -Mg + Mg_5Gd + $Mg_{24}Y_5$ gradually increases, and the Y content has almost no effect on the solidification and solid solution regions of Mg-Gd alloys. However, it can be seen from Figure 4b that two eutectoid reaction points appeared in α -Mg with the introduction of the Zr element with higher thermal conductivity, and as its content increased from 0.1 wt.% to 0.2 wt.%, and α -Mg \rightarrow $Mg_{24}Y_5$ + Mg_5Gd , the eutectoid transformation reaction point of $Mg_{24}Y_5$ + Mg_5Gd shifts to the right, and the solid solution range of α -Mg decreases, which significantly affects the precipitation temperature of each precipitation phase.

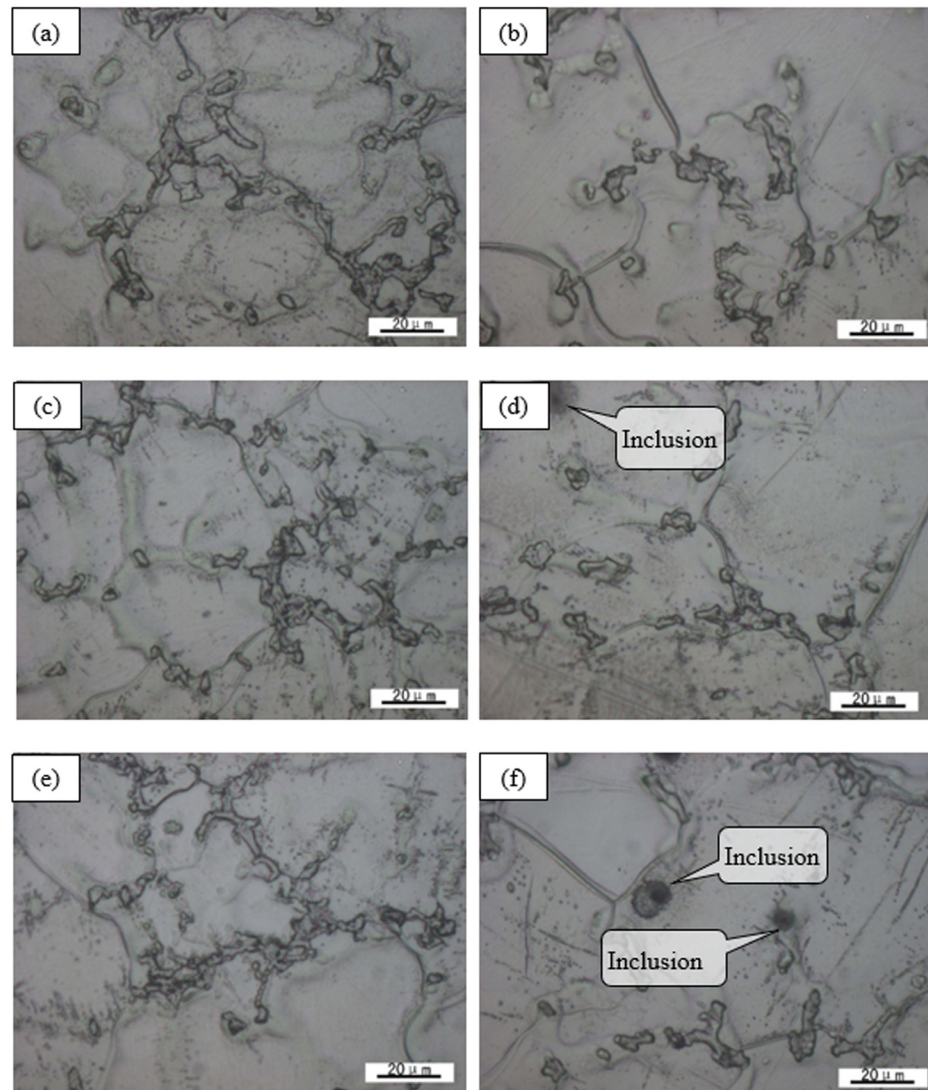


Figure 3. Optical microstructure of GWK alloys with different composition: (a,b) the center and edge of GWK-a ingot; (c,d) the center and edge of GWK-b ingot; (e,f) the center and outside of GWK-c ingot.

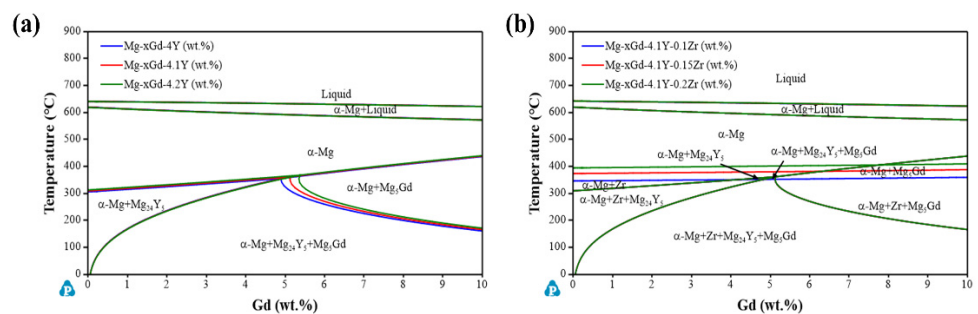


Figure 4. Effect of (a) yttrium and (b) zirconium on equilibrium phase diagram of the Mg-Gd based alloys.

Figure 5 shows the solidification and precipitation behavior of different alloys. It is not difficult to find that the solidification interval and room temperature phase composition and content of different alloys are similar, but due to the different additions of Zr, compared with GWK-b (Figure 5b), GWK-c (Figure 5c), GWK-a (Figure 5a) alloy has a wider solid solution range, which means that it is easier to achieve the ideal solid solution effect through

heat treatment. In conclusion, the precipitation behavior of Mg-Gd-Y-Zr (GWK) alloys is not sensitive to the addition of the element Y, but is extremely sensitive to the addition of the element Zr. Therefore, in order to obtain a better homogenization effect, it is necessary to control the addition amount of Zr.

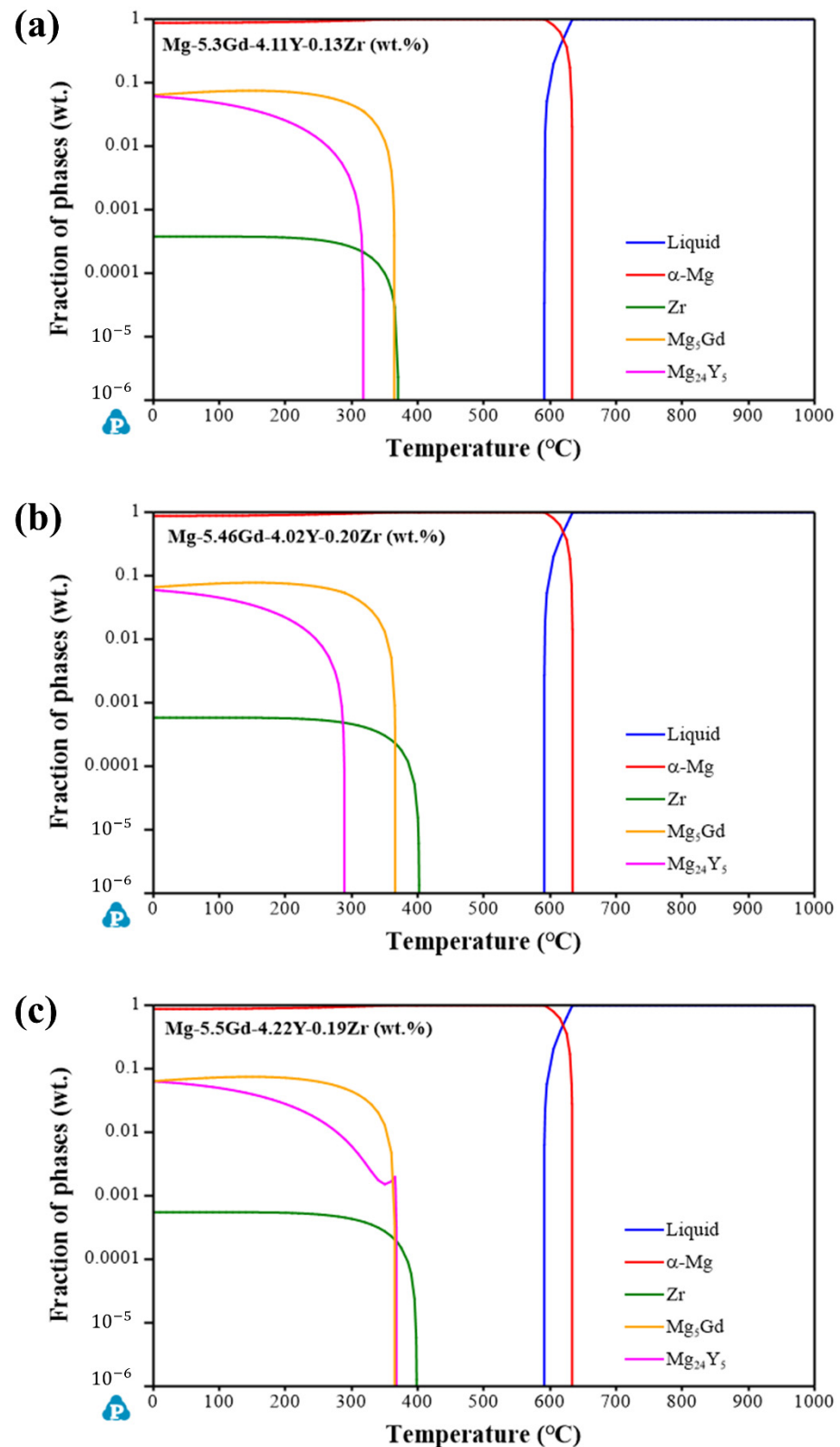


Figure 5. Solidification behavior of (a) GWK-a; (b) GWK-b; (c) GWK-c alloys.

Figure 6 shows the optical microstructure of GWK-a alloy under different homogenization treatment specifications. The comparison shows that after homogenization treatment at 480 °C/6 h, the second phase is significantly reduced, and the structure segregation is significantly improved. The annealing temperature is low, the atomic diffusion is insufficient, less than one-third of the eutectic compound remains at the grain boundary, and a small amount of undissolved phase still exists in the grain; after solution treatment at 500 °C/6 h, the alloy exhibits equiaxed grains, compared with 480 °C, the undissolved material in the crystal is significantly reduced, the segregation is basically eliminated and only a small amount of high-temperature insoluble phase remains at the grain boundary, and the grain size does not change significantly. After 520 °C/6 h treatment, the grain structure is abnormal. It grows upwards, and due to long-term high temperature treatment, irregularly aggregated overfired remelting products appear in the crystal. After the alloy is over-fired, the low-melting eutectic remelts and solidifies on the grain boundary and in the matrix, which changes the compact state of the structure before over-burning, and deteriorates the structure continuity, mechanical properties, fatigue and corrosion properties of the alloy. Since the over-burning of the alloy cannot be eliminated by means of heat treatment or thermomechanical processing, the pre-extrusion homogenization treatment process of the GWK alloy is comprehensively considered to be 500 °C/6 h.

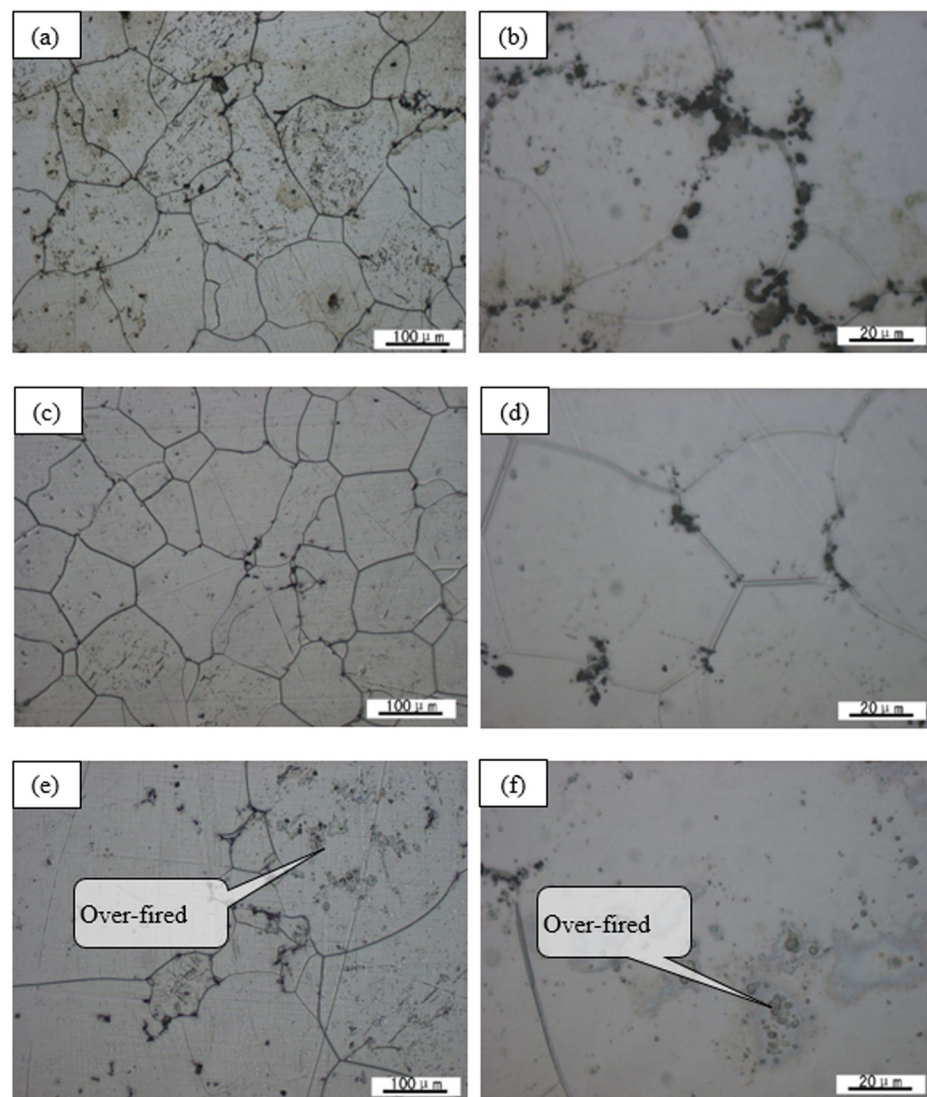


Figure 6. Optical microstructure of GWK-a alloy upon various homogenization temperature for 6 hs: (a,b) 480 °C; (c,d) 500 °C; (e,f) 520 °C.

3.3. Microstructure of Extruded Alloy

Hot working can refine the grains, make the coarse structure broken and evenly distributed, and can also improve the defects such as pores and porosity generated in the casting, so that the inclusions generally distributed along the grain boundaries in the as-cast state are distributed in a fibrous shape along the deformation direction. All factors help to further improve the room temperature mechanical properties of the alloy. Figure 7 shows the metallographic structure of the cross-section of different GWK alloy hot extrusion bars. Under this process (the preheating temperature of the billet is 430–450 °C, the preheating temperature of the die is 430 °C, and the extrusion ratio is 25), the alloys are almost completely equal to each other. Axial recrystallized grains have a grain size between 20 and 30 μm. There is only a small amount of island-shaped or ellipsoidal residual intermetallic compounds on the grain boundaries. By comparing the homogenized structure in the previous text, it can be judged that this is the high melting point phase remaining after solid solution. The aforementioned inclusions are not obvious. It is speculated that the inclusions are extruded during extrusion. During the process, it is broken and dispersed at the grain boundaries of the recrystallized structure.

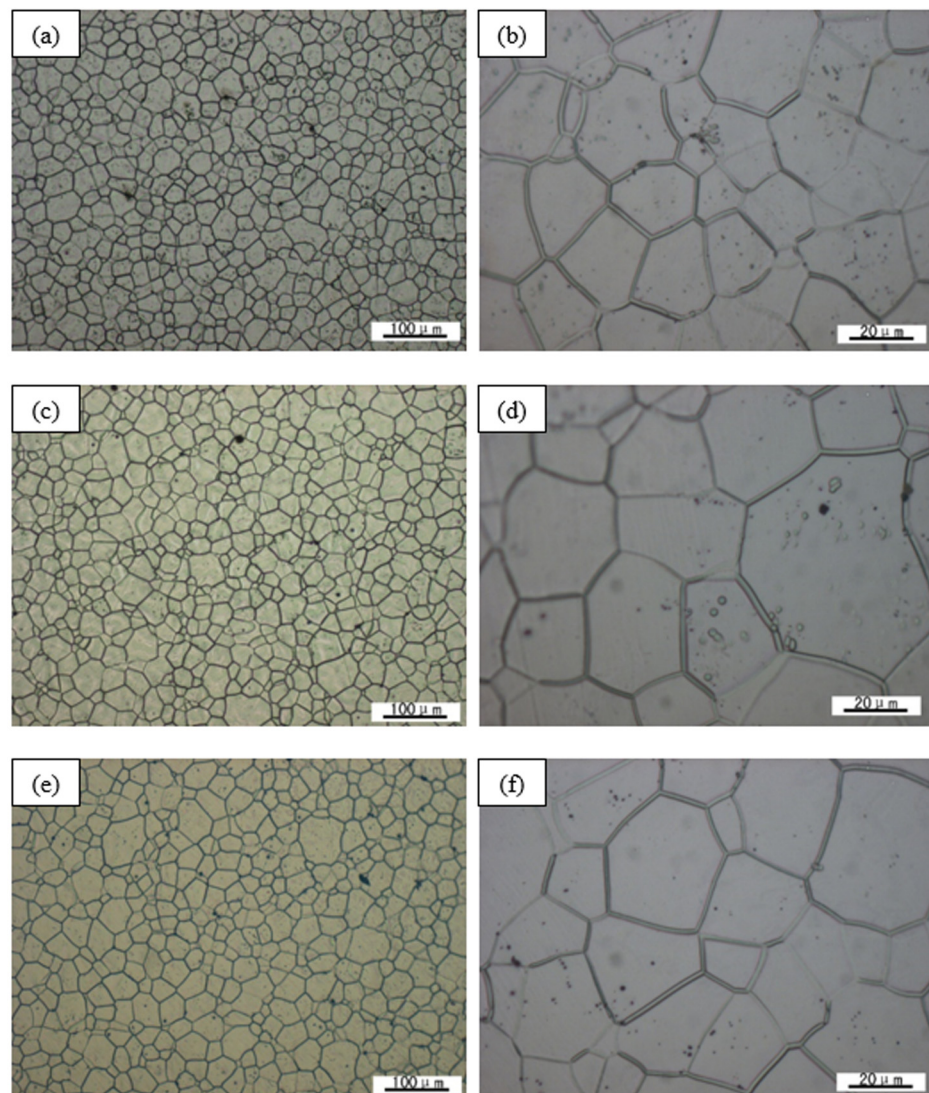


Figure 7. Optical microstructure of as-extruded GWK alloys: (a,b) GWK-a; (c,d) GWK-b; (e,f) GWK-c alloy.

In addition, to further study the effect of different extrusion ratios on the microstructure, the related results are shown in Figure 8. When the extrusion ratio (R) is 25, the recrystallization of the alloy is relatively complete, showing a uniform equiaxed grain structure; while when the extrusion ratio is 17, the grain size in the alloy structure is different, and the grain size is different. Significantly increased, the recrystallization effect is poor. This is mainly due to two reasons: First, the strains introduced by different extrusion ratios are different. The average strain ($=\ln(R)$) corresponding to the extrusion ratio of 25:1 is 3.2, which is higher than the average corresponding to the extrusion ratio of 17:1. The strain of 2.8 is favorable for dynamic recrystallization; secondly, a high extrusion ratio means more deformation heat generation, and high temperature is also favorable for dynamic recrystallization. It is worth noting that, for magnesium alloys whose mechanical properties are strongly dependent on the grain size, the extruded grain size has an important influence on the subsequent heat treatment.

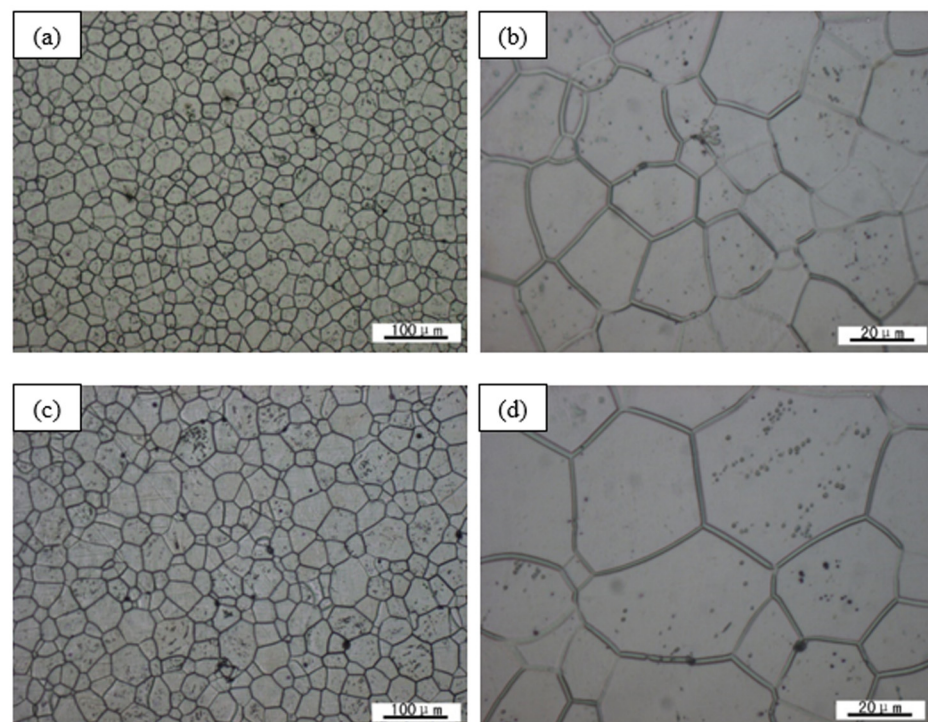


Figure 8. Optical microstructure of as-extruded GWK-a alloy with different extrusion ratio: (a,b) 25:1; (c,d) 17:1.

3.4. Microstructure of Aging Alloy

In order to find out the effect of the aging process on the microstructure of the as-extruded GWK alloy, the aforementioned GWK-a alloy with an extrusion ratio of 25 was selected for further analysis. Figure 9 shows the metallographic structure of the as-extruded GWK-a alloy after different aging treatments. Compared with Figure 8a,b before aging, it can be seen that after aging at 200 °C/12 h (Figure 9a,b), in the microstructure a large number of agglomerates and rod-shaped second phases and a small amount of dot-shaped black phases were precipitated in the middle. After 24 h (Figure 9c,d), the second phase of lumps and rods decreased significantly compared to 12 h, while the black phase of dots did not increase significantly; when the aging time reached 64 h (Figure 9e,f), in the lumps The rod-shaped second phase disappeared completely, and it can be concluded that the second phase is a low melting point phase. When the bar is extruded and air-cooled, these second phases are solid-dissolved in the matrix before precipitation, and the driving force provided by the temperature rise in the early stage of aging causes them to be precipitated from the structure; however, long-term heat preservation provides solid solutions. Thermodynamic

conditions, after slow and long-term diffusion between atoms, eventually all disappear. The black dot-like phase existing in the 64 h structure is the high melting point strengthening phase. After the aging time increases to 72 h (Figure 9g,h), the precipitation of the high melting point strengthening phase increases significantly, showing an over-aging state.

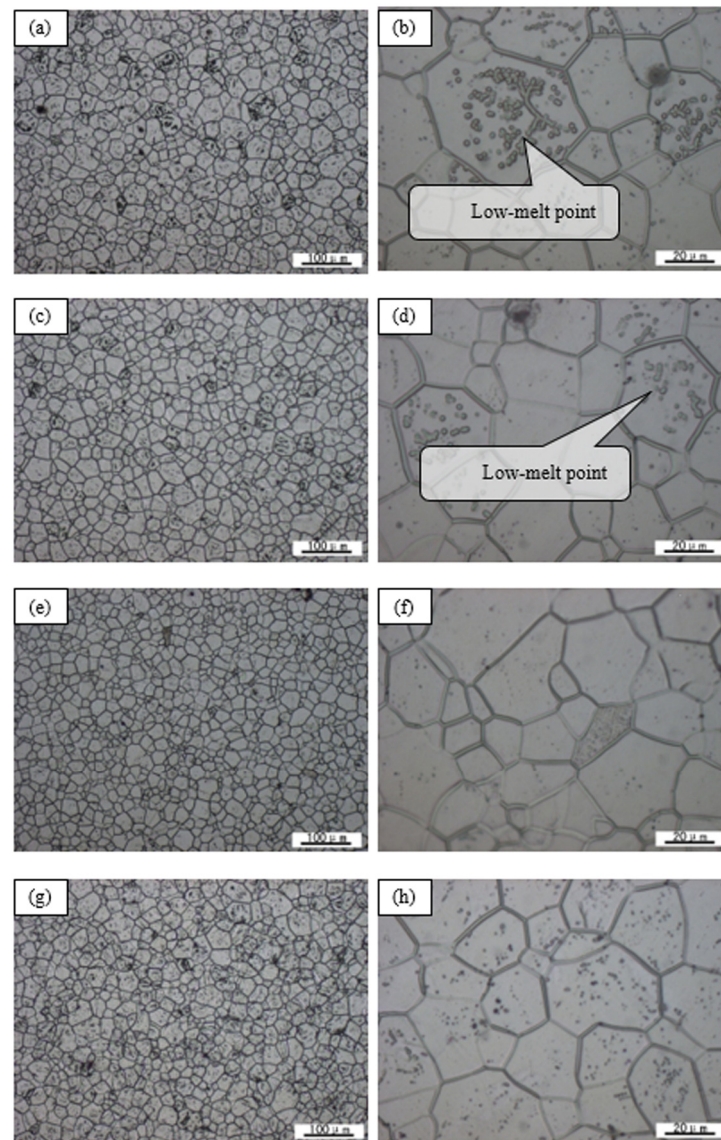


Figure 9. Optical microstructure of as-extruded GWK-a through different aging process (a,b) 200 °C/12 h; (c,d) 200 °C/24 h; (e,f) 200 °C/64 h; (g,h) 200 °C/72 h.

Vostry [21] studied the decomposition process of α -Mg supersaturated solid solution (S.S.S.S.) of Mg-15 wt.%Gd alloy under isochronous annealing conditions at 20–500 °C, and showed that it appeared a typical three-stage aging precipitation: S.S.S.S (cph) \rightarrow β'' (D0₁₉) \rightarrow β' (cbco) \rightarrow β (Mg₅Gd, fcc). The aging precipitation sequence of Mg-Y binary alloy [22,23] presents the following three stages: S.S.S.S. (cph) \rightarrow β'' (cbco) \rightarrow β' (cbco) \rightarrow β (Mg₂₄Y₅, bcc). However, some scholars [24] believe that the three-stage aging of Mg-Gd-Y ternary alloy is S.S.S.S. \rightarrow β'' (D0₁₉) \rightarrow β' (cbco) \rightarrow β (bcc), that is, the later stage is the same as the Mg-Y binary alloy phase. Similarly. But more studies show that [25–28] in Mg-Gd-Nd, as well as Mg-Dy-Nd and Mg-Y-Nd-based alloys, a four-stage aging precipitation sequence, namely S.S.S.S. (cph) \rightarrow β'' (D0₁₉) \rightarrow β' (cbco) \rightarrow β 1(fcc) \rightarrow β (fcc), shows the under-aging, half-peak aging, peak aging and over-aging stages. Combined with the above analysis, it can be seen that after 12 h, 24 h, 64 h and 72 h aging treatment of GWK-a alloy, the aging stage

covers four stages: under-aging, half-peak aging, peak aging and over-aging, which is consistent with the reported research results [29,30].

3.5. Normal Temperature Mechanical and Combustion Performance Test of Alloy

Due to the low diffusion activation energy of magnesium alloys, natural aging is generally not possible. Considering the large difference in the solid solubility of elements Gd and Y in magnesium at high and low temperature in this study, direct aging treatment was used to improve the mechanical properties of the alloy at room temperature. Table 2 shows the room temperature mechanical properties of the hot-extruded bar of GWK-a alloy in the state. Combining Figure 9 and Table 2, it can be seen that compared with the as-cast alloy, the mechanical properties of the alloy after hot extrusion are significantly improved, which is mainly caused by the grain refinement accompanying the recrystallization process. As the aging treatment progresses, the tensile strength (UTS) and yield strength (YS) of the alloy gradually increase with aging time, and reach a peak at 64 h: that is, the tensile strength is 405 MPa and the yield strength is 275 MPa, and then the elongation decreased gradually from 15% in the extruded state to 6% at 72 h. Combined with Figure 9g,h in the previous section, when the alloy is aged at 200 °C/72 h, the precipitates inside the material begin to grow and the spacing increases, and the macroscopic manifestation of overaging is the deterioration of the material strength.

Table 2. Tensile properties of as-cast, as-extruded and as-aged GWK alloys at room temperature.

GWK-a Alloy	UTS (Rm/MPa)	YS (R _{P0.2} /MPa)	El. (A%)	Modulus E/G/B (GPa)
As-cast	228.35 ^{+2.4} _{-1.9}	133.7 ^{+2.6} _{-1.1}	8.3 ^{+0.4} _{-0.3}	41.9 ^{+0.7} _{-0.4} /16.4 ^{+0.2} _{-0.1} /27.6 ^{+0.5} _{-0.2}
As-extruded	272.69 ^{+5.5} _{-3.6}	172.7 ^{+4.8} _{-3.0}	15.25 ^{+2.0} _{-1.2}	
As-aged 200 °C/12 h	296.7 ^{+3.8} _{-2.9}	192.8 ^{+5.6} _{-2.1}	10.67 ^{+2.8} _{-1.5}	
As-aged 200 °C/24 h	306.7 ^{+2.0} _{-3.4}	199.7 ^{+3.5} _{-4.3}	9.72 ^{+2.3} _{-4.2}	
As-aged 200 °C/64 h	405 ^{+5.3} _{-0.8}	275 ^{+1.8} _{-3.2}	8.12 ^{+1.7} _{-2.4}	43 ^{+0.9} _{-0.3} /17.5 ^{+0.3} _{-0.5} /28.3 ^{+0.7} _{-0.4}
As-aged 200 °C/72 h	392.5 ^{+6.7} _{-3.4}	292.1 ^{+1.7} _{-0.5}	5.92 ^{+1.6} _{-0.7}	

In addition, from Table 2, it can be seen that the hot extrusion of Φ19 mm bar die and then artificial aging treatment for 64 h can effectively release the strength and toughening potential of GWK-a alloy, thereby obtaining high-strength and tough magnesium alloy materials. At the same time, the elastic modulus, shear modulus and bulk elastic modulus of the alloy after aging treatment are not much different from those of the as-cast alloy, because the elastic modulus of the material is only related to the chemical composition of the material, and has nothing to do with its microstructure changes and the heat treatment state.

Figure 10a,b shows the flame retardancy test results of different as-cast alloys (GWK-a and GWK-c), and the as-cast alloys cannot ignite within 2 min, and the burning sample self-extinguished within 3 min after turning off the burner, which meets the demand of a qualified flammability sample according to the FAA standard [10]. Figure 10c,d shows the photos of the flame retardant samples of the extruded and aged GWK-a alloys after the flame retardant test. Additionally, the aged GWK-a sample remains more longer in size than the extruded GWK-a through the flame retardancy test, which also implies that it has lower weight loss of the sample and better flame retardant properties. After comparing their lengths, it can be seen that the aged alloy exhibits exceptionally excellent flame retardant properties.

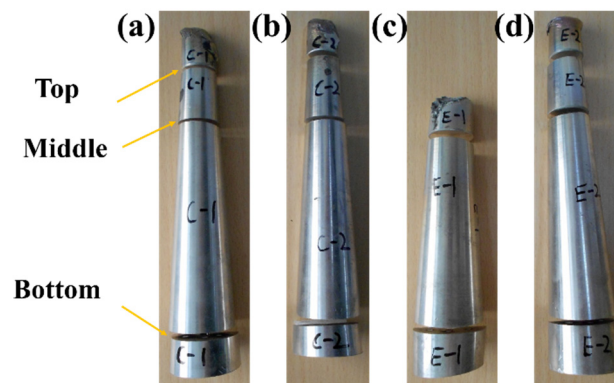


Figure 10. Flammability testing results and corresponding photos showing cutting locations of (a,b) as-cast GWK-a and GWK-c alloys; (c,d) as-extruded and aged (200 °C/64 h) GWK-a alloys.

Figure 11 shows the optical microstructures of the top, middle, and bottom of the flame retardant test samples of GWK-a and GWK-c as-cast alloys. It is not difficult to see that the dendrites at the top burned part basically disappear compared to the unburned parts in the middle and bottom. Some equiaxed crystals appear and the second phase is greatly reduced, which indicates that during the combustion process, due to the intense heating of the top contact flame, the microstructure exhibits a certain degree of solid solution effect. Since GWK-a contains more Y elements than GWK-c alloy, when the Mg-Gd-Y-Zr alloy is oxidized at high temperature, it is mainly composed of relatively chemically active Y which is more stable and dense after the MgO cracks. The Y_2O_3 oxide film prevents further combustion from occurring. Therefore, the flame retardancy of GWK-a as-cast alloy is slightly improved.

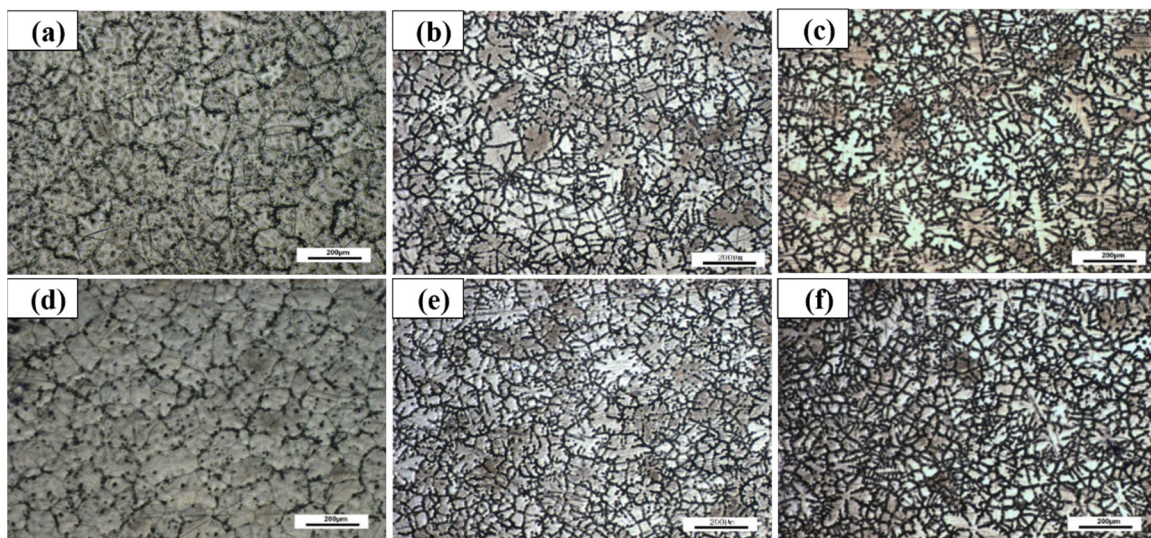


Figure 11. Optical microstructure from the top, middle, bottom of as-cast (a–c) GWK-a and (d–f) GWK-c alloys after flammability test.

Figure 12 shows the microstructures of the GWK-a extruded and aged alloy flame retardant test samples at different sampling positions. Comparing the bottom microstructures, it can be found that due to the influence of temperature gradients at different positions in the combustion test, the bottom microstructure of the extruded alloy is relatively partial and low-melting precipitation phases appear in the original structure, while the aged alloys contain more high-melting secondary phases with slightly higher grain size. Take the extruded and aged samples equidistant from the burning extinction point of the respective samples for microstructure observation and analysis. As shown in Figure 12a,c, the second phase

in the two grains has basically been dissolved and extruded. The grains of the as-stated alloys are relatively finer after combustion, which indicates that the grain boundaries may also have a certain influence on the flame retardant properties. In addition, comparing the structure of the alloy in the middle and bottom of the burning sample in the aging state, as shown in Figure 12d,e, the structure uniformity is good, and the grain size and the content of the second phase are basically the same.

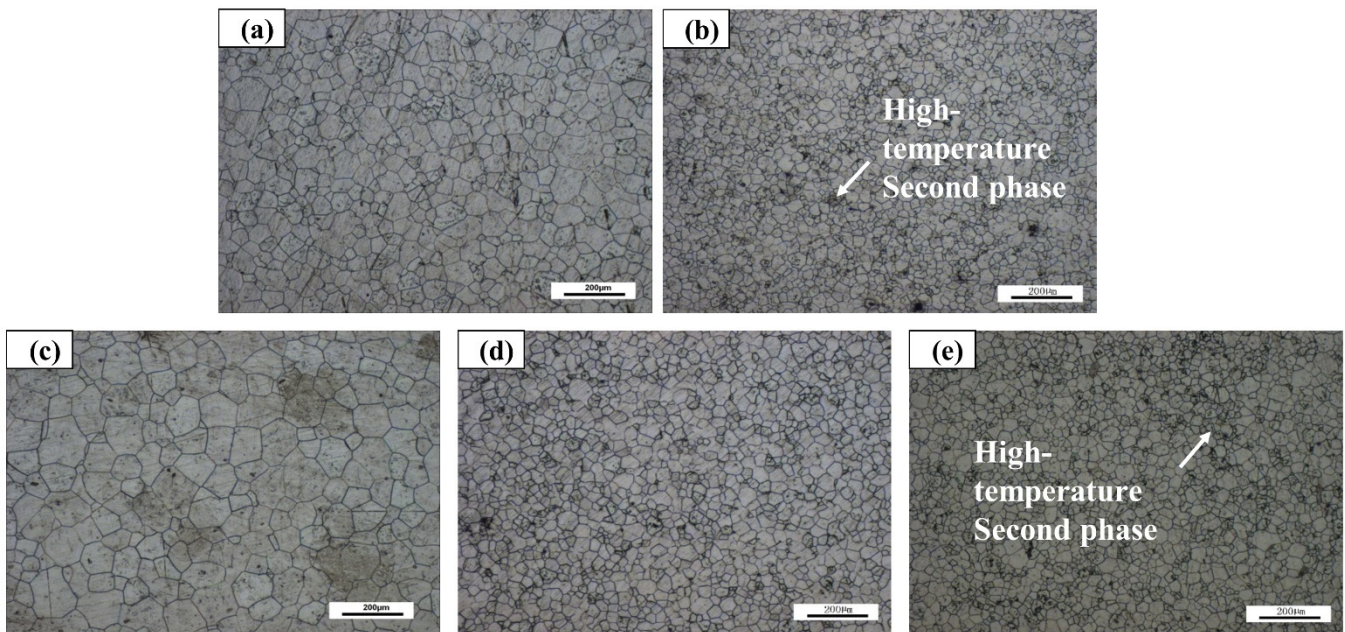


Figure 12. Optical microstructure from the top, middle, bottom of (a,b) as-extruded and (c–e) aged GWK-a alloy after flammability testing.

Combined with the flammability test results, it can be seen that under the heating of high temperature gradient and high energy density, the rare-earth content of extruded alloy shows obvious component segregation. Due to the sharp reduction of rare-earth elements and rare earth second phase in the solid solution of magnesium matrix, its high-temperature oxidation resistance and ignition point are greatly reduced; spontaneous combustion starts at lower temperature and short heating and lasts for quite a long time, showing relatively poor flame retardant performance. As for the as cast alloy, combined with the influence of Y and Zr content on its precipitation behavior, as shown in Figure 4, it is not difficult to speculate that GWK-c alloy is easier to precipitate rare-earth phase under high temperature gradient than GWK-a alloy, especially because the Y-containing rare-earth phases leads to Y deficiency in the matrix, which may delay the formation of yttrium oxide protective film during combustion, but its precipitation behavior is basically similar to the rare-earth content at the combustion. Therefore, the difference of flame retardancy is not obvious.

4. Conclusions

In this paper, GWK magnesium alloys with different compositions were successfully prepared by hot extrusion, and their microstructure, mechanical properties and flame retardant properties under different states were characterized and evaluated, and the following main conclusions were obtained:

- (1) The alloy has good casting characteristics, uniform distribution of ingot elements, and stable yield of main alloy elements. The outer microstructure of the alloy is finer than the core microstructure, and the second phase is finely dispersed. The size and distribution of the alloy phases of different compositions are similar, which verifies the reliability of the semi-continuous casting production quality.

- (2) The optimal homogenization treatment specification of the alloy is 500 °C/6 h. If the temperature is too low, the atomic diffusion is insufficient, and the eutectic compound and the refractory phase are distributed in the grain boundary and within the grain, respectively. If the temperature is too high, the grain will grow abnormally and burnt out.
- (3) After the alloy was subjected to an extrusion temperature of 430 °C, an extrusion speed of 3–5 mm/s, an extrusion ratio of 25, and an artificial aging treatment of 200 °C/64 h, the tensile strength was 405 MPa, and the yield strength was 275 MPa. the elongation was 8.12%.
- (4) The flame retardant properties of the alloys are closely related to the elements and their addition amounts. The as-cast alloys have little difference in the flame retardant properties; while the extruded alloys have flame retardant properties due to uneven precipitation behavior under high temperature gradient and high energy density heating. Poor; aging alloys exhibit excellent flame retardant properties due to pre-precipitation of high temperature refractory phases.

Author Contributions: Conceptualization, J.F.; Data curation, Y.Q. and W.Y.; Formal analysis, W.Y.; Investigation, X.D.; Methodology, Y.Q. and Y.Z.; Project administration, J.F. and H.Y.; Supervision, H.Y.; Visualization, X.D.; Writing—original draft, Y.Q.; Writing—review & editing, Y.Z. All authors have read and agreed to the published version of the manuscript.

Funding: This work was supported by the National Natural Science Foundation of China (51701060) and Funding Project for Introduced Overseas Students of Hebei Province of China (C20190505), High-level Talent Funding Project of Hebei Province of China (100410).

Conflicts of Interest: The authors declare no conflict of interest.

References

1. Pan, F.; Zhang, J.; Wang, J.; Yang, M.; Han, E.; Chen, R. Key R&D activities for development of new types of wrought magnesium alloys in China. *Trans. Nonferrous Met. Soc. China* **2010**, *20*, 1249–1258.
2. Jiang, B.; Zeng, X.; Song, J. Development Strategies for China's Advanced Magnesium Alloy Industry Toward 2035. *Chin. J. Eng. Sci.* **2020**, *22*, 76–83.
3. National Natural Science Foundation of China, Chinese Academy of Sciences. *Materials Science of China's Discipline Development Strategy in the Next 10 Years*; Science Press: Beijing, China, 2012.
4. Zhang, D. Thoughts on the Development Strategy of my country's Magnesium Alloy Industry. *World Nonferrous Met.* **2004**, *7*, 4–20.
5. Ding, W.; Zeng, X. Development and application of Mg materials in China. *Chin. J. Met.* **2010**, *46*, 1450–1457.
6. Prasad, S.V.S.; Prasad, S.B.; Verma, K.; Mishra, R.K.; Kumar, V.; Singh, S. The role and significance of Magnesium in modern day research-A review. *J. Magnes. Alloy.* **2021**, *10*, 1–61. [[CrossRef](#)]
7. Gradinger, R.; Gneiger, S.; Betz, A. Investigations on Fire-Resistant Magnesium Alloys for Aerospace Applications. *Mater. Sci. Forum* **2015**, *828*, 492–498. [[CrossRef](#)]
8. Czerwinski, F. Controlling the ignition and flammability of magnesium for aerospace applications. *Corros. Sci.* **2014**, *86*, 1–16. [[CrossRef](#)]
9. Tan, Q.; Atrens, A.; Mo, N.; Zhang, M. Oxidation of magnesium alloys at elevated temperatures in air: A review. *Corros. Sci.* **2016**, *112*, 734–759. [[CrossRef](#)]
10. U.S. Department of Transportation, Federal Aviation Administration. *Evaluating the Flammability of Various Magnesium Alloys During Laboratory—and Full-Scale Aircraft Fire Tests*; Federal Aviation Administration: Atlantic City, NJ, USA, 2013.
11. Yang, Y.; Xiong, X.; Chen, J.; Peng, X.; Chen, D.; Pan, F. Research advances in magnesium and magnesium alloys worldwide in 2020. *J. Magnes. Alloy.* **2021**, *9*, 705–747. [[CrossRef](#)]
12. Tan, Q.; Yin, Y.; Mo, N.; Zhang, M. Recent understanding of the oxidation and burning of magnesium alloys. *Surf. Innov.* **2019**, *7*, 71–92. [[CrossRef](#)]
13. Wang, W.; Wang, W.; Wang, Q.; Zhang, M.; Wang, A.; Li, M. Flame resistance and oxidation behavior of Mg-Y-Ce-Zr alloys. *Mater. Res. Express* **2018**, *6*, 016536. [[CrossRef](#)]
14. Qin, L.; Ding, J.; Fang, Z.; Zhao, W. Effect of Ce Addition on the Ignition-Proof Properties and Surface Tension of AZ91D-2.5Ca (Wt.%) Magnesium Alloy. *Mater. Sci. Forum.* **2014**, *788*, 82–87. [[CrossRef](#)]
15. Tan, Q.; Mo, N.; Jiang, B.; Pan, F. Combined influence of Be and Ca on improving the high-temperature oxidation resistance of the magnesium alloy Mg-9Al-1Zn. *Corros. Sci.* **2017**, *122*, 1–11. [[CrossRef](#)]

16. Inoue, S.-I.; Yamasaki, M.; Kawamura, Y. Oxidation behavior and incombustibility of molten Mg-Zn-Y alloys with Ca and Be addition. *Corros. Sci.* **2019**, *149*, 133–143. [[CrossRef](#)]
17. Bian, M.; Huang, X.; Chino, Y. Improving flame resistance and mechanical properties of magnesium–silver–calcium sheet alloys by optimization of calcium content. *J. Alloy. Compd.* **2020**, *837*, 155551. [[CrossRef](#)]
18. Li, R.G.; Li, H.R.; Pan, H.C.; Xie, D.S.; Zhang, J.H.; Fang, D.Q.; Dai, Y.Q.; Zhao, D.Y.; Zhang, H. Achieving exceptionally high strength in binary Mg-13Gd alloy by strong texture and substantial precipitates. *Scr. Mater.* **2021**, *193*, 142–146. [[CrossRef](#)]
19. Wan, Y.; Tang, B.; Gao, Y.; Tang, L.; Sha, G.; Zhang, B.; Liang, N.; Liu, C.; Jiang, S.; Chen, Z.; et al. Bulk nanocrystalline high-strength magnesium alloys prepared via rotary swaging. *Acta Mater.* **2020**, *200*, 274–286. [[CrossRef](#)]
20. Cao, W.; Chen, S.L.; Zhang, F.; Wu, K. Pandat software with PanEngine, PanOptimizer and PanPrecipitation for multi-component phase diagram calculation and materials property simulation. *CAPHAD Comput. Coupling Phase Diagr. Thermochem.* **2009**, *31*, 328–342. [[CrossRef](#)]
21. Vostry, P.; Smola, B.; Stulíková, I.; von Buch, F.; Mordike, B.L. Microstructure Evolution in Isochronally Heat Treated Mg-Gd Alloys. *Phys. Status Solidi* **1999**, *175*, 491–500. [[CrossRef](#)]
22. Zhu, C.; Chen, B. Atomic Scale Investigation on Precipitates and Defects of Mg-RE Alloys: A Review. *Adv. Eng. Mater.* **2018**, *21*, 1800734. [[CrossRef](#)]
23. Solomon, E.L.S.; Marquis, E.A. Deformation behavior of β' and β''' precipitates in Mg-RE alloys. *Mater. Lett.* **2018**, *216*, 67–69. [[CrossRef](#)]
24. Smola, B.; Stulíková, I.; Buch, F.V.; Mordike, B.L. Structural aspects of high performance Mg alloys design. *Mater. Sci. Eng. A* **2002**, *324*, 113–117. [[CrossRef](#)]
25. Zheng, K.Y.; Dong, J.; Zeng, X.Q.; Ding, W. Precipitation and its effect on the mechanical properties of a cast Mg-Gd-Nd-Zr alloy. *Mater. Sci. Eng. A* **2008**, *489*, 44–54. [[CrossRef](#)]
26. Zheng, K.Y.; Dong, J.; Zeng, X.Q.; Ding, W. Effect of pre-deformation on aging characteristics and mechanical properties of a Mg-Gd-Nd-Zr alloy. *Mater. Sci. Eng. A* **2008**, *491*, 103–109. [[CrossRef](#)]
27. Li, D.; Dong, J.; Zeng, X.; Lu, C. Transmission electron microscopic investigation of the $\beta_1 \rightarrow \beta$ phase transformation in a Mg-Dy-Nd alloy. *Mater. Charact.* **2010**, *61*, 818–823. [[CrossRef](#)]
28. Gao, Y.; Liu, H.; Shi, R.; Zhou, N.; Xu, Z.; Zhu, Y.M.; Nie, J.F.; Wang, Y. Simulation study of precipitation in an Mg-Y-Nd alloy. *Acta Mater.* **2012**, *60*, 4819–4832. [[CrossRef](#)]
29. Li, Y.; Qu, C.; Wang, J.; Xu, R. Exceptional aging hardening behaviour of nanocrystalline Mg-Y-Nd-Gd-Zr alloy prepared by high pressure torsion. *J. Alloy. Compd.* **2020**, *813*, 152123. [[CrossRef](#)]
30. Guo, Y.; Liu, B.; Xie, W.; Luo, Q.; Li, Q. Anti-phase boundary energy of β series precipitates in Mg-Y-Nd system. *Scr. Mater.* **2021**, *193*, 127–131. [[CrossRef](#)]